LARGE-EDDY SIMULATION OF THE TURBULENT FLOW OVER A FLAT PLATE AT SMALL INCIDENCE

Luiz Eduardo Bittencourt Sampaio
Dept. Mech. Eng., PUC-Rio, Rua Marquês de São Vicente,225 22453-900, Rio de Janeiro - RJ - Brasil
luizebs@mec.puc-rio.br

Angela Ourivio Nieckele
Dept. Mech. Eng., PUC-Rio, Rua Marquês de São Vicente,225 22453-900, Rio de Janeiro - RJ - Brasil
nieckele@mec.puc-rio.br

Abstract. Turbulent flow over a flat plate at small incidence angle is a challenging problem, since it presents many complex structures and regimes such as boundary layer separation, recirculation, reattachment, vortices breakdown, to mention just a few. The recirculation bubble formed just behind leading edge is particularly critical. Unlike structures observed at greater incidence angle, it is extremely turbulent and anysitropic. Attempts have been made to numerically simulate such flow with Reynolds Average Navier-Stokes (RANS) methods, but none of them has yet been proved satisfactory. Large eddy simulation is then an attractive solution to represent its complexity, since far more structures are resolved compared to RANS. In this paper we present the general characteristics of the problem, numerical formulation and methodology used, as well as some preliminar results obtained with a coarse mesh using the open source code FOAM. Altough still far from the accuracy expected from such methodology, these initial results not only allowed some conclusions on the physics of the problem, as it has also helped define some directives for future works in relation to spatial and time discretization.

Keywords. Turbulent, Large-eddy simulation, flat plate, small incidence anlge.

1. Introduction

Turbulent flow over a flat plate at shallow incidence is a complex situation. It has been investigated both numerically (Collie et al., 2003) and experimentally (Crompton, 2000), but it is still not completely understood. Among several interesting regimes and structures encountered in this problem, one can cite separation of the boundary layer, reattachment, vortices breakdown, and, the most challenging one, the recirculation bubble formed right behind the leading edge. The latter structure is essentially turbulent for high Reynolds numbers, unlike other shorter bubbles formed in airfoils, which may stay laminar for about 60 percent of the bubble length (Breuer & Jovicic, 2001, Mary, 2003). Moreover these bubbles are very thin for incidences lower than 5 degrees, which makes them strongly anisotropic and unstable structures.

Figure 1. Physics of the Problem.

For incidences lower than 5 to 7 degrees there is a reattachment point over the plate, which splits the flow in two branches - one continuing downstream, towards the trailing edge, and the other returning to the leading edge, and then completing the bubble. The former carries some turbulent structures downstream, which has been generated in the leading edge bubble. These structures directly influence the development of the downstream boundary layer, the recovery region of the plate, and, in cases of curved plates with strongly adverse pressure gradient, they may dictate further separations.

The importance of the thin layer bubble is two fold. Firstly, it is responsible for a low-pressure peak right behind the leading edge, which is the main contributor to the total plate lift and drag. Secondly, its influence is experienced all over the downstream flow, through the turbulent structures detached from the bubble. Particularly, the interaction between leading edge bubble and trailing edge separation is still not completely understood (Collie et al. 2003). Therefore, accurate capturing of this bubble is crucial to the overall comprehension and prediction of the turbulent flow over a thin plate at shallow incidence.

Collie et al. (2003) tried to numerically predict the flow behavior using RANS models and showed they were not suitable to represent this kind of flow. The authors suggest a Large-eddy simulation should be more accurate in capturing these complex structure and regimes.

In this paper a preliminary numerical investigation of the problem is presented. It is restricted to incompressible flow over a flat plate at small incidence angle, using Large Eddy Simulation. This is the first step to analyze thin curved plates flows, which is our final goal.

2. Basic LES Equations

The number of degrees of freedom to be solved in Navier-Stokes equations must be reduced in order to make simulations feasible with nowadays computer resources. With this aim, a filtered variable can be defined as (Sagaut, 2002):

$$\bar{f}(\vec{x},t) = \int_D f(\vec{x}',t) G(\vec{x},\vec{x}',\overline{\Delta}) d\vec{x}' , \tag{1}$$

being $f(\vec{x}',t)$ the original variable, $\bar{f}(\vec{x},t)$ the filtered variable, and $G(\vec{x},\vec{x}',\overline{\Delta})$, the filter function with bandwith $\overline{\Delta}$. Applying this filter to Navier-Stokes and continuity equations and assuming that the filtering operations commute with derivatives, it is obtained:

$$\frac{\partial \bar{u}_i}{\partial t} + \frac{\partial}{\partial x_j}\left(\overline{u_i u_j}\right) = -\frac{1}{\rho_o}\frac{\partial \bar{p}}{\partial x_i} + \upsilon \frac{\partial^2 \bar{u}_i}{\partial x_j \partial x_j} \quad , \tag{2}$$

$$\frac{\partial \bar{u}_i}{\partial x_i} = 0 , \tag{3}$$

where $\bar{u}_i$ is the ith component of the resolved velocity vector, x_i are the coordinates, $\bar{p}$ is the resolved pressure and υ the cinematic viscosity.

Rewriting the convective part in terms of available variables, $\bar{u}_i$, the Navier-Stokes equation can be rewritten as:

$$\frac{\partial \bar{u}_i}{\partial t} + \frac{\partial}{\partial x_j}\left(\bar{u}_i \bar{u}_j\right) = -\frac{1}{\rho_o}\frac{\partial \bar{p}}{\partial x_i} - \frac{\partial \tau_{ij}}{\partial x_j} + \upsilon \frac{\partial^2 \bar{u}_i}{\partial x_j \partial x_j} \quad , \quad \tau_{ij} = \overline{u_i u_j} - \bar{u}_i \bar{u}_j \tag{4}$$

being τ_{ij} is the sub-grid tensor, to be modeled. According to Boussinesq hypothesis, this tensor may be assumed to represent a macroscopic, turbulent mixture, in analogy to microscopic, laminar one. Therefore, it may be written as:

$$\tau_{ij} = -\upsilon_{SGS}\left(\frac{\partial \bar{u}_i}{\partial x_j} + \frac{\partial \bar{u}_j}{\partial x_i}\right) + \frac{2}{3}k\delta_{ij} , \tag{5}$$

where υ_{SGS} is the effective, sub-grid viscosity, representing the turbulent sub-grid mixture process, and k is the generalized sub-grid kinetic energy, defined as the half-trace of the sub-grid tensor, which can be incorporated in the pressure term.

Several models have been proposed to compute this sub-grid viscosity (Sagaut, 2002). At the present work, the one equation model of Yoshizawa e Horiuti (1985), which express the viscosity as a function of a filtered sub-grid kinetic energy q_{SGS}^2, has been selected,:

$$\upsilon_{SGS} = \sqrt{\frac{2}{3}}\frac{A}{\pi K_0^{3/2}}\overline{\Delta}\sqrt{q_{SGS}^2} = C_2 \overline{\Delta}\sqrt{q_{SGS}^2} \tag{6}$$

$$q_{SGS}^2(\vec{x},t) = \frac{1}{2}\overline{\left(u_i'(\vec{x},t)\right)^2} = \frac{1}{2}\overline{\left(u_i(\vec{x},t) - \bar{u}_i(\vec{x},t)\right)^2} \tag{7}$$

This model is expected to be superior to Samagorisk model (Sagaut, 2002), once it incorporates information of the non-resolved scales to evaluate υ_{SGS}, allowing representation of non-equilibrium turbulent structures. Since this information is not explicitly available from the filtered Navier-Sokes equations, an evolution equation must be derived for q_{SGS}^2, which is ultimately the quantity synthesizing information in scales below cut-off. This can be done by first subtracting the filtered N-S equations from its unfiltered version, then multiplying the result by $u_i'(\vec{x},t)$ and finally filtering again. The following transport equation is therefore obtained:

$$\frac{\partial q_{SGS}^2}{\partial t} = \frac{\partial\left(\bar{u}_j q_{SGS}^2\right)}{\partial x_j} - \frac{1}{2}\frac{\partial\left(\overline{u_j' u_i' u_i'} + \overline{u_j u_i' u_i'}\right)}{\partial x_j} - \frac{\partial\left(\overline{u_j p}\right)}{\partial x_j} + \frac{\partial}{\partial x_j}\left(\upsilon\frac{\partial q_{SGS}^2}{\partial x_j}\right) - \upsilon\left(\overline{\frac{\partial u_i'}{\partial x_j}\frac{\partial u_i'}{\partial x_j}}\right) + \frac{\partial\left(\bar{u}_i \tau_{ij}\right)}{\partial x_j} - \tau_{ij}\frac{\partial \bar{u}_i}{\partial x_j} \tag{8}$$

Some of its terms still cannot be computed and have to be modeled. Following McComb (1990), it is assumed that the nonlinear diffusive term is proportional to the gradient of the sub-grid kinetic energy, known as Kolmogorov-Prandtl relation and the dissipative term is rewritten based on dimensional analysis, yielding

$$\frac{\partial}{\partial x_j}\left(\frac{1}{2}\overline{u'_j u'_i u'_i} + \overline{u'_j \, \overline{p}}\right) = C_2 \frac{\partial}{\partial x_j}\left(\overline{\Delta}\sqrt{q^2_{SGS}}\,\frac{\partial q^2_{SGS}}{\partial x_j}\right) \quad ; \tag{9}$$

$$\varepsilon = \frac{\upsilon}{2}\left(\overline{\frac{\partial u'_i}{\partial x_j}\frac{\partial u'_i}{\partial x_j}}\right) = C_1 \frac{\left(q^2_{SGS}\right)^{3/2}}{\overline{\Delta}} \tag{10}$$

Eventually, the final transport equation is obtained:

$$\frac{\partial q^2_{SGS}}{\partial t} = -\underbrace{\frac{\partial\left(\overline{u}_j\, q^2_{SGS}\right)}{\partial x_j}}_{I} - \underbrace{\tau_{ij}\overline{S}_{ij}}_{II} - \underbrace{C_1\frac{\left(q^2_{SGS}\right)^{\frac{3}{2}}}{\overline{\Delta}}}_{III} + \underbrace{C_2\frac{\partial}{\partial x_j}\left(\overline{\Delta}\sqrt{q^2_{SGS}}\,\frac{\partial q^2_{SGS}}{\partial x_j}\right)}_{IV} + \underbrace{\upsilon\frac{\partial^2 q^2_{SGS}}{\partial x_j^2}}_{V} \tag{11}$$

Its terms have the following physical interpretation: I – advection by the resolved scales; II – production by the resolved scales; III – turbulent dissipation; IV – turbulent diffusion; V – viscous dissipation. The emperical constants are $C_1 = 1$ e $C_2 = 0.1$ in accordance with Yoshizawa (1985 e 1991) and Horiuti (1985).

3. Numerical Method

A Large Eddy simulation was performed to investigate the flow over the inclined flat plate. To this end, an open source code, called FOAM from Nabla ltda. (Fureby 1998), has been selected. It is based on Finite Volume Method, with second order spatial discretization scheme (Jasak 1996). As for time advances, an Implicit first-order scheme (Euler) has been chosen, in which the next step is computed based on information on the most recent available time, which, together with spatial discretization, generates a system of equations to be solved, representing the transport of momentum. An iterative method, BiCCG - Bi-Conjugate Cholesky preconditioned Gradient (Golub e Van Loan, 1996) - has been used to solve this system.

The pressure-velocity coupling was handled by the PISO algorithm (Pressure Implicit Split Operator, Issa, 1985). The resulting algebraic system was solved with the ICCG iterative algorithm (Incomplete Cholesky preconditioned Gradient, Golub e Van Loan, 1996). Before each time-step, the sub-grid tensor field is updated, based on the one equation model described in item 2.

4. Results

The geometry and domain set up used are shown in Fig. (2). They were defined in accordance with the work of Collie et al (2003), where suitability of RANS models for this class of flows has been investigated. Therefore, a direct comparison between LES and RANS is addressed here.

The flat plate is 160mm in length, 6mm thick and has a knife leading edge in 20 degree angle, exactly as in the experimental investigation of Crompton et al. (2000) and RANS investigation by Collie et al (2003). Since LES implies 3D Navier-Stokes solution, a third dimension (z) was added, corresponding to a wingspan of 5cm. The computational domain expands in 8×19×0.3125 box, in chord units (c).
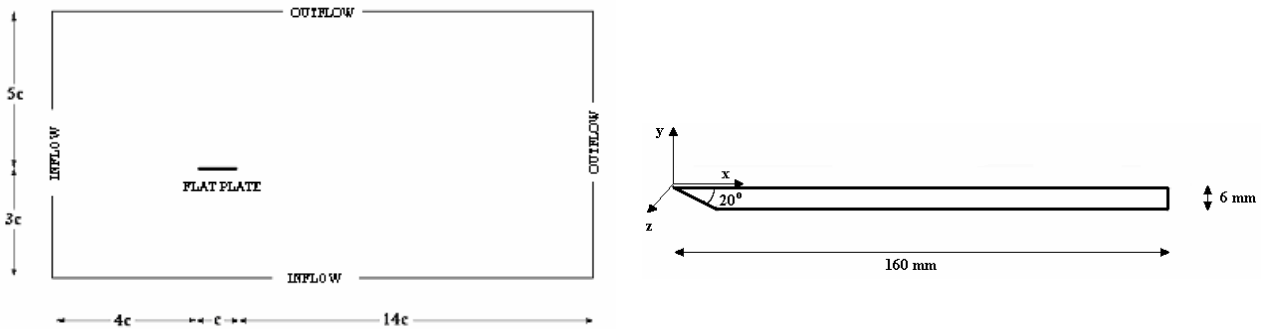
Figure 2. Domain and detail of the plate geometry.

As far as boundary condition is concerned, null sub-grid kinetic energy and null velocities (no slip conditions) were prescribed at the walls, constant velocity and null kinetic energy at in inflow faces, and null velocity and kinetic energy diffusion at outflow faces. The incidence angle is thus determined by the constant velocity vector imposed at the inflow boundary. Particularly in this work, the x and y velocity components were set as 10m/s and 0.5241m/s respectively, corresponding to an incidence angle of 3 degrees, for which there is still a reattachment of the separated flow at the plate surface.

Considering air properties, the above plate dimensions and the operational speed, the resulting chord-based Reynolds number is above 10×10^5, for which, according to Crompton (2000) the flow becomes Reynolds independent. Table (1) lists the main parameters involved in the simulation.

The mesh is presented in Fig. (3). Approximately 91600 control volumes were defined (concentrating near the walls), however only 10 subdivisions were specified in the wingspan direction. Along the plate length 55 grids were specified, resulting in 1100 control volume over the plate surface.
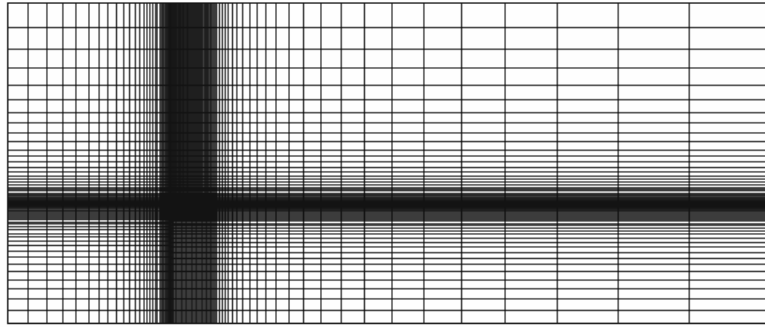
(a) Computational Domain.
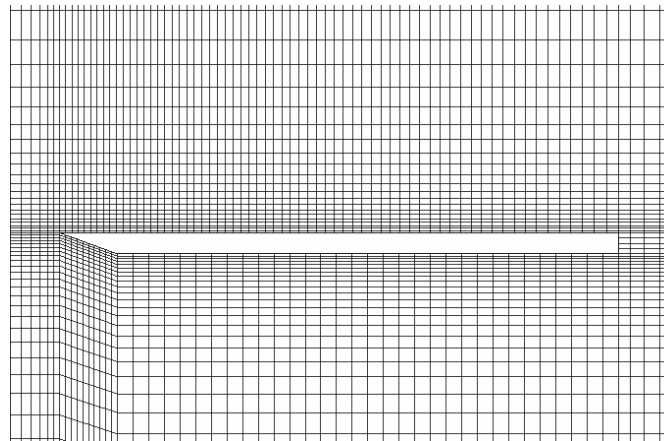
(b) Detail near plate

Figure 3. Mesh

Table 1 – Simulation Parameters

Processing type	Property 1 (%)
Free stream velocity magnitude (m/s)	10.0
Incidence Angle (deg)	3
Time step (s)	$1\ 10^{-5}$
Air cinematic viscosity (m^2/s)	$1.4\ 10^{-5}$
Wingspan (cm)	10

The time evolution of pressure and velocity was examined at three different locations, in order to determine when statistical steady state has been established. Figure (4) illustrates the location of the three probes in the neighbourhood of the plate. The pressure evolution is shown in Fig. (5). It can be seen that up to 0.05 s, there is a strong increase on the pressure values. After approximately 0.2 s, it can be considered that, at least for first order statistics, that a steady state has been reached, although the pressure oscillation is large. During this time (0.2 seconds), a particle immersed on the recirculation bubble is able to complete more than 12 turns-around, if one considers a bubble perimeter of about 16cm, i.e., a bubble that extend half the chord, and with an average speed of the same order of the free stream velocity (10m/s).
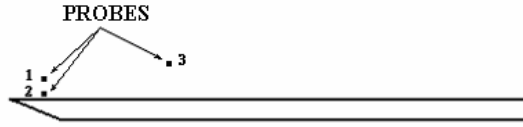
Probe Number	Coordinates (x, y, z) (in chord units, c)
Probe 1	(0.0625, 0.03125, 0.3125)
Probe 2	(0.0625, 0.00625, 0.3125)
Probe 3	(0.3125, 0.06250, 0.3125)

Figure 4. Probes location.
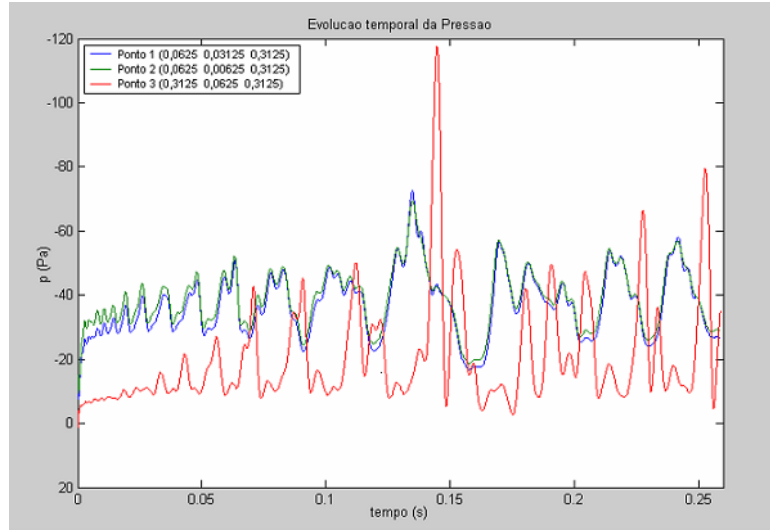
Figure 5. Pressure time evolution.

Temporal spectrum of the sampled signal pressures have also been computed and are shown in Fig. (6), together with a rough estimative of frequencies cut-off, based on mesh spacing. To estimate frequency cut-off, it was admitted that the temporal correlation is entirely governed by the advection of spatial structures with their correlation length over the point in consideration. Therefore, a possible way of obtaining a temporal frequency cut-off in terms of a grid spacing is:

$$\omega_c = 2\pi f_c = \cong \frac{2\pi \overline{U}}{L} \tag{12}$$

where f_c is the cut frequency, L and $\overline{U}$ are the mesh spacing and mean velocity component corresponding to the largest ω_c.

Table 2 shows location and estimated frequency cut-off for each probe. Note that only the frequency cut-off for probe 2 lies within represented range of spectrum.

Table 2 – Probes location and frequency cut-off

Probes	Location (mm)	Δx (mm)	Δy (mm)	Δz (mm)	Ux (m/s)	Uy (m/s)	Uz (m/s)	ωc (rad/s)
Probe 1	(10, 5, 50)	1,83	1,17	10	11	2,4	0	37800
Probe 2	(10, 1, 50)	1,83	0,70	10	-0,8	0	0	2700
Probe 3	(50, 10, 50)	2,28	1,98	10	13	2,8	0	36000

A straight line representing the −5/3rd Kolmogorov´s law is also shown in Fig. (6). A small discrepancy is observed between the results obtained from the large-eddy simulation and the theory. This may be due to a too coarse mesh in the wingspan direction, leading to a misrepresentation of the three dimensional characteristic of the turbulent flow. It is convenient to remember that in 2D flow, turbulent structures take longer to decorrelate in comparison to 3D flows, simply because there is no vortex stretching mechanism to transfer energy from the big-scales to small ones, where dissipation takes place. Longer correlation times translate in frequency to narrow and consequently steeper spectrum. Therefore, although nominally 3D LES is being solved, the three dimensional aspects of the flow are not well captured,

since the grid definition in the z direction is still not enough to capture the vortex stretching mechanism in its completeness. As a result, the spectrum slope observed is a little below the theory.

The total sampled time for these spectrum calculations was 0.89 seconds, yielding a frequency resolution of $\omega_R = 2\pi f_R = 2\pi/0.89$ rad/s = 7.1 rad/s, as can be confirmed in the figures.
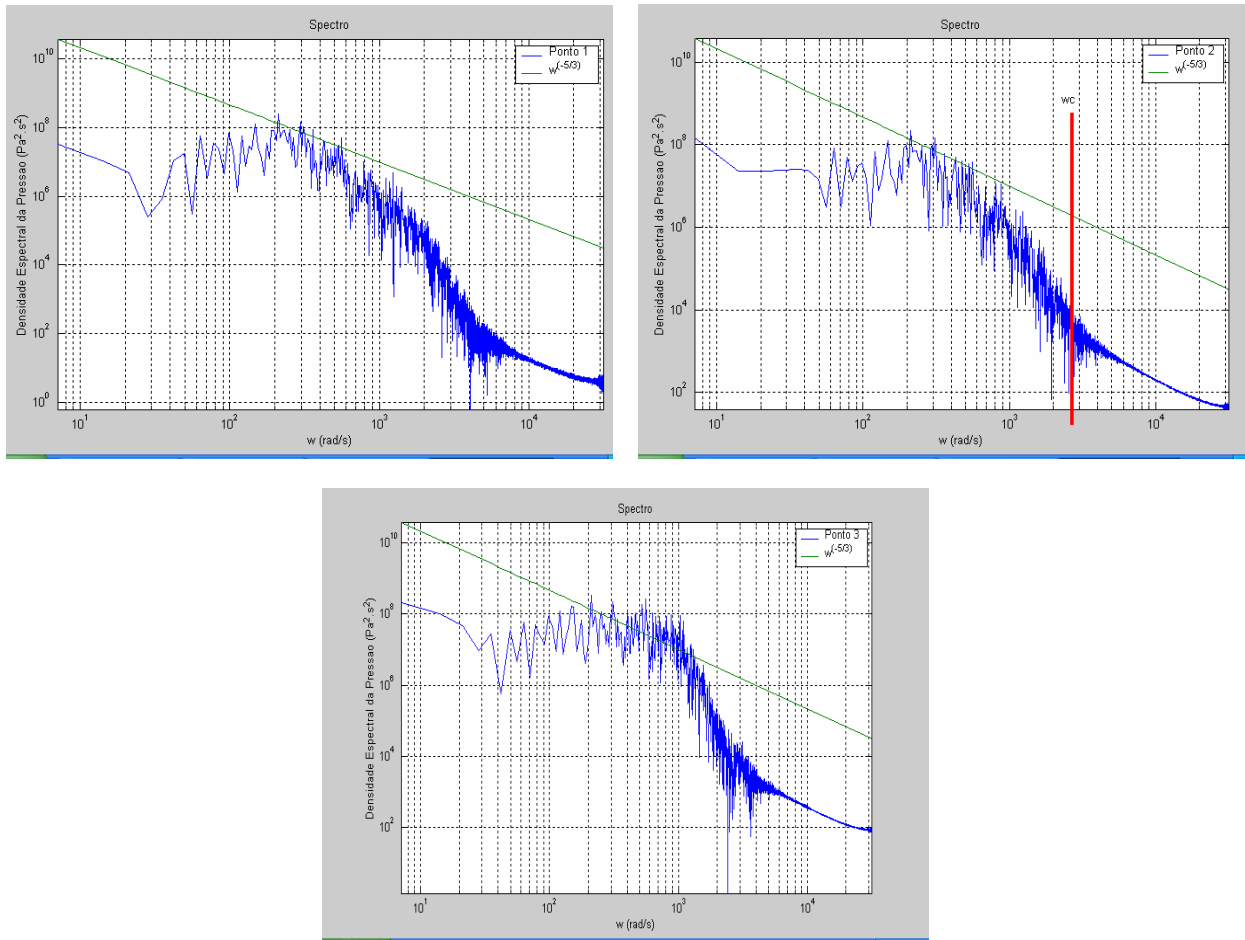
Figure 6. Pressure temporal spectrum.

A snapshot of the flow taken at 0.1 seconds at half wingspan is reproduced at Fig. (7) It reviews a principal recirculation bubble formed right behind the leading edge, and some vortices along the plate length, detached from this main structure. In Fig. (7) all arrows representing the velocity have the same length, but are coloured according to the velocity magnitude of its location.
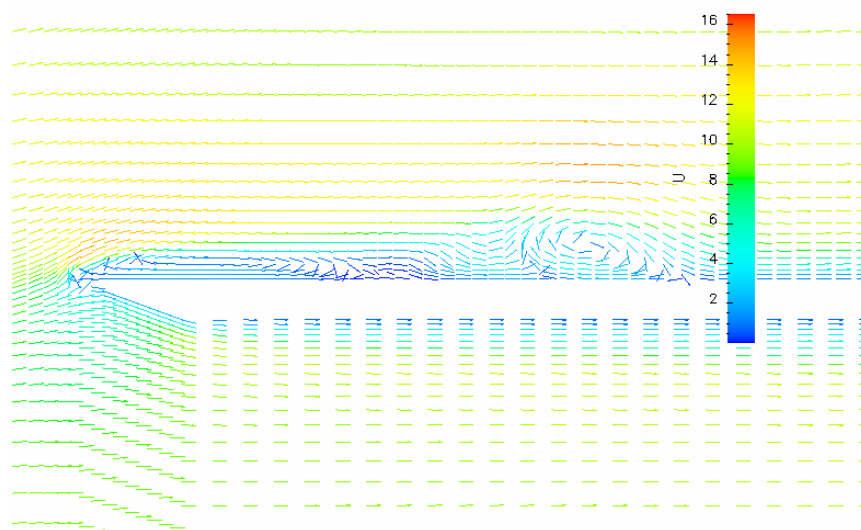
Figure 7. Velocity field snapshot at 0.1 seconds.

It is also interesting to note a flow deflection below the plate to form a stagnation point in the bottom surface of the edge, which is ultimately responsible for the well-determined boundary layer separation. Indeed, irrespective of boundary layer development and transition, the point of separation is always in the extreme point of the knife leading edge, due to the fact that the flow accelerating from the separation point will encounter an abrupt transition there.

Figure (8) helps visualize how pressure and velocity field correlates in the same instant of time. Both fields are superposed, being pressure information displayed as contours coloured by intensity, while velocity are represented by vectors of the same size, coloured by magnitude. Subsequent snapshots reviews that these low pressure bubbles and eddies structures are carried together by the main flow along the top region of the plate, while the main bubble close to leading edge stays in place. Again, variables were taken at half wingspan, which it was verified to be very representative, since no z-variation greater than one percent have been detected for any variable in the whole wingspan. Therefore, unless otherwise noticed, all figures in this paper are based in half wingspan values.
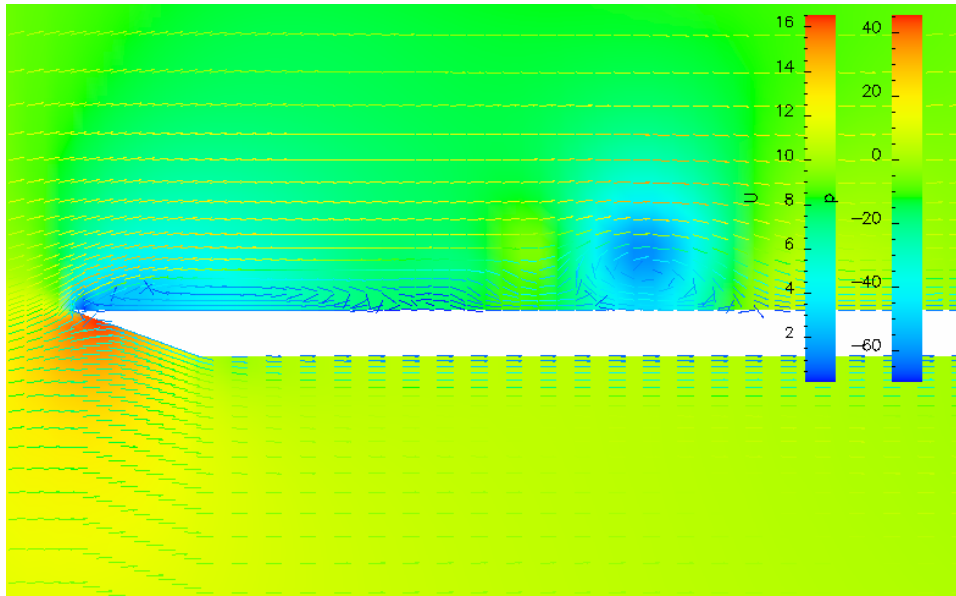
Figure 8. Pressure and Velocity field snapshot at 0.1 seconds.

The coherent characteristic of the main bubble in contrast to the detached ones can be better viewed when a time average is taken on the velocity field, as in Fig. (9). There, one can see that only the main bubble survives the average processing, thus indicating its coherency.
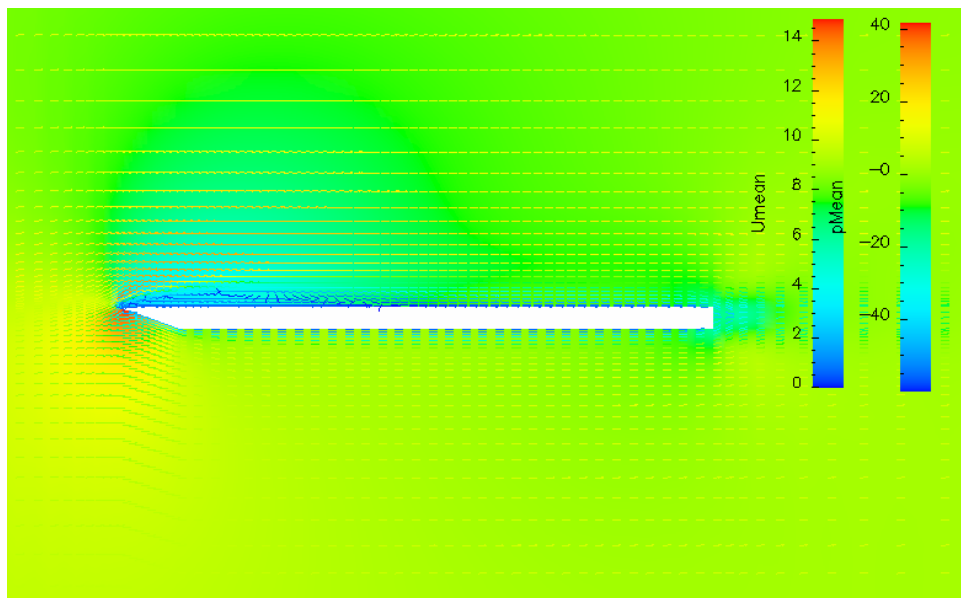
Figure 9. Mean Pressure and Velocity field.

The pressure coefficient along the plate is shown at Fig.(10), where a reverse scale has been employed. There is a steep variation near the leading edge. The pressure attains a minimum and then its is recovered along the plate. Near the trailing edge another pressure reduction can be seen.

By examining the mean pressure field, Fig. (9) together with the pressure coefficient, Fig. (10), it is clearly seen why the leading edge recirculation is so important for the total lift of the plate. There is a very low-pressure region over the top surface of the plate, which spans over a considerable part of the plate length.
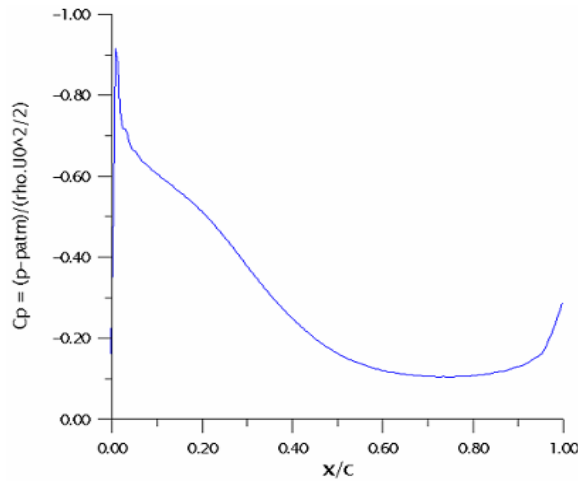
Figure 10. Pressure Coefficient.

Figure (11) depicts the corresponding velocity profiles taken at x/c = 0.031, 0.125, 0.25, and 0.375, compared to the results obtained by Collie et al. (2003) using two RANS models (two equations model k-ω and stress tensor equations model SST). The experimental data of Crompton (2000) are also presented. The results are qualitatively similar, but neither the RANS results nor the present LES results present an excellent agreement. Further the large-eddy simulations did not present better results than the RANS models in the bubble region, which is certainly due to the coarseness of the mesh. However, at regions away from this structure and from the top surface of the plate, the results are very encouraging. Therefore, it is expected that with a finer mesh a full representation of the boundary layer structures will be obtained.
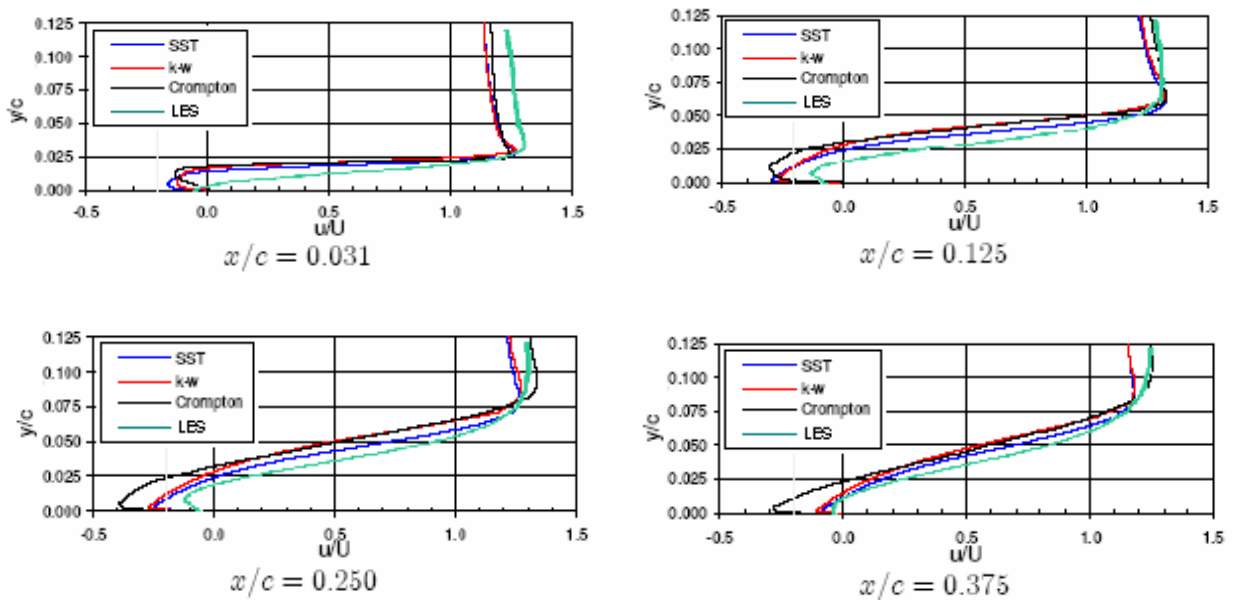
Figure 11. Mean x-Velocity profile.

Another interesting issue to be examined is how an initially two-dimensional flow develops into a turbulent, three-dimensional one. It is well known that a rectilinear vortex filament is an unstable structure and tends to bend, leading to non-null z-components of velocity. This has been extensively studied in other classical separated flows, such as the flow around a circular cylinder (Catalano et al., 2003). Therefore, it is expected rectilinear filaments of vortices to be detached from the leading edge bubble and then carried by the main stream along the top of the plate. As they are transported, they start to bend until they reach a complete chaotic state further downstream. Then, it is expected that the

z velocity component in the neighbourhood of the main bubble to be weaker than in it at further downstream regions, as confirmed by Fig. (12).
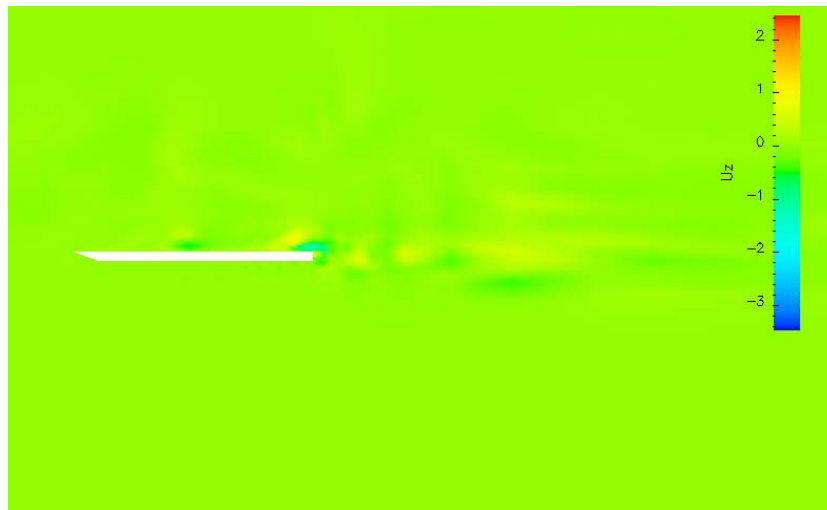
Figure 12. Instantaneous z-velocity.

5. Final remarks

The present preliminary simulations allowed some interesting conclusions on the physical aspects of the flow. It was possible to discriminate between coherence structures that contribute to the averaged field, like the main leading edge bubble, and the non-coherent eddy structures carried by the principal stream, which cancels out in the average process. However, the mesh resolution employed must be refined to better capture the turbulent structures. A mesh refinement is needed close to the wall and in the wingspan direction. Further other schemes for time advances (explicit ones of higher order) must be selected along with shorter time steps, to increase the solution accuracy.

The evolution from a two-dimensional flow to a turbulent three-dimensional one could also be observed, suggesting that an increase along x-coordinate on the number of wingspan subdivisions may be an effective way of representing the three-dimensionality of the flow without sacrificing too much computational costs.

6. Acknowledgement

7. References

Breuer, M and Jovicic, N., 2001, "Separated Flow Around A Flat Plate At High Incidence: An LES Investigation", J. Turbulence vol. 2, pp. 18

Catalano, P., Wang, M.Iaccarino, G. And Moin, P. 2003, "Numericla Simulation of the Flow Around a Circular Cylinder at High Reynolds Numbers", Int. J. of Heat and Fluido Flow, v. 24, pp. 463-469.

Collie, S., Jackson, P. S., Gerritsen, M., 2003, "Turbulence Modelling Of The Flat Plate At Shallow Incidence", Yacht Research Unit, University of Auckland, Private Bag 92019, Auckland, New Zeland.

Crompton, M. J., e Barret, R. V., 2000, "Investigation Of The Separation Bubble Formed Behind The Sharp Leading Edge Of A Flat Plate At Incidence", Proc. Instn Mech. Engrs, v. 134 Part G.

Fureby, C., Jasak, H., Tabora, G, Weller, H. G., 1998, "A Tensorial Approach To Computational Continuum Mechanics Using Object-Oriented Techniques", Computers in Physics, v.12, No. 6.

Golub, G. H., Van Loan, C. F., 1996, "Matrix Computations", Third Edition, Johns Hopkins.

Issa, R., 1985, "Solution of the Implicit Discretized Fluid Flow Equations by Operator-Splitting", Journal of Computational Physics, v. 62, pp. 40-65.

Jasak, H. 1996. "Error Analysis and Estimation for the Finite Volume Method with Applications to Fluid Flows", Dr. Eng. Thesis, PhD University of London and Diploma of Imperial College, Department of Mechanical Engineering, Imperial College of Science, Technology and Medicine, UK (English).

Mary, I, 2003, "Large Eddy Simulation of Vortex Breakdown Behind a Delta Wing", Int. J. Heat and Fluid Flow, v. 24, pp. 596-605.

McComb, W. D., 1990, "The Physics Of Fluid Turbulence", Clarendon Press, Oxford.

Sagaut, P., 2002, "Large Eddy Simulation for Incompressible Flows, An Introduction", Springer, Second Edition.

Yoshizawa, A., Horiuti, K., 1985, "A Statistically-Derived Subgrid-Scale Kinetic Energy Model For The Large-Eddy Simulation Of Turbulent Flows", Journal of Physics Society Japan, v. 54(8), pp. 2834-2839.